



## Article

# Wind Effects on a Permeable Double Skin Façade, the ENI Head Office Case Study

Giulia Pomaranzi <sup>\*</sup> , Ombretta Bistoni, Paolo Schito, Lorenzo Rosa  and Alberto Zasso

Department of Mechanical Engineering, Politecnico di Milano, Via G. La Masa 1, 20156 Milan, Italy; ombretta.bistoni@polimi.it (O.B.); paolo.schito@polimi.it (P.S.); lorenzo.rosa@polimi.it (L.R.); alberto.zasso@polimi.it (A.Z.)

\* Correspondence: giulia.pomaranzi@polimi.it

**Abstract:** Currently, the energy and environmental efficiency of buildings has led to the development of cladding systems that may help to reduce the structure's energy demand, using techniques such as the Permeable Double Skin Façade (PDSF). Given complex aerodynamic interactions, the presence of an external porous screen in addition to an inner skin may play a crucial role in the fluid-dynamic characterization of such buildings, making the definition of wind effects very complex. A new methodology for the quantitative assessment of the impact of wind-loading conditions on this particular type of cladding is presented. It is based on a combined experimental–numerical approach, essentially based on wind-tunnel tests on a rigid scale model and computational fluid dynamic simulations. A case study is proposed as an application of this methodology. Results include the design pressure values for the inner glazed façade and the permeable facade. An estimation of the flow rate across the porous skin is quantified using the numerical model.

**Keywords:** permeable double skin; cladding load; porosity; CFD; porous media model



**Citation:** Pomaranzi, G.; Bistoni, O.; Schito, P.; Rosa, L.; Zasso, A. Wind Effects on a Permeable Double Skin Façade, the ENI Head Office Case Study. *Fluids* **2021**, *6*, 415. <https://doi.org/10.3390/fluids6110415>

Academic Editor: Luca Patruno

Received: 14 September 2021  
Accepted: 22 October 2021  
Published: 16 November 2021

**Publisher's Note:** MDPI stays neutral with regard to jurisdictional claims in published maps and institutional affiliations.



**Copyright:** © 2021 by the authors. Licensee MDPI, Basel, Switzerland. This article is an open access article distributed under the terms and conditions of the Creative Commons Attribution (CC BY) license (<https://creativecommons.org/licenses/by/4.0/>).

## 1. Introduction

Energy-efficiency strategies are presently integrated into the design process of a building. The façade may play an important role in the reduction of the system's energy demand by significantly decreasing solar radiation and increasing the inhabitants' living comfort. Permeable double skins are an example of high-efficiency façades where the building envelope consists of two façades (or skins): the inner one is usually made of glass panels and the outer skin is characterized by a porous metallic screen. The first goal of this kind of cladding is to protect the building from direct sunlight, with the external skin acts as a louvre, allowing a nearly unobstructed view of the outside.

As far as interaction with wind is concerned, the presence of an outer permeable skin is expected to alter the distribution of wind-induced pressure on the inner façade and, thus, the design cladding loads. In addition, strong wind effects are expected on the external mesh, as it is the first layer exposed to wind action. The porous layer may act as a sheltering device for the inner façade, implying a potential reduction of the design pressure for the latter. When predicting the wind effects on a building envelope of this type, a typical multi-scale problem must be addressed—the relevant effects due to the building's geometry being immersed in the atmospheric boundary layer must be considered along with those related to the small-scale details of the porous components' geometry. Both scales simultaneously affect the building-wind interaction.

Despite the popularity of this cladding system in recent architectural trends, the structural design of permeable cladding in terms of wind effects has been sparsely studied in current literature [1]. The effects of wind-loading conditions on a porous façade have been studied by Gerhardt and Janser [2], who investigated the pressure distribution on a rainscreen installed over a closed façade. They highlighted the reduction of the wind-induced pressure on the inner skin, compared to a single-layer façade, and the net load

expected on the permeable elements. However, these results refer to a very low value of porosity (in the order of 1%) compared to typical values applied for the PDSF (20–50%). More recently, Kemper et al. [3] proposed different wind-load recommendations for rectangular-shaped buildings with single porous cladding and a porous double skin façade. For the latter, the porous cladding elements are made using stainless steel wire mesh with 20% porosity. Both full-scale measurements and wind tunnel tests on a scale model were performed to address the aerodynamic behaviour of the porous skin and corresponding wind loads. Pomaranzi et al. [4,5] and Lo et al. [6] quantified the reduction of the wind-induced pressure experienced by the inner sealed façade when an outer porous screen was installed, by proposing a comparative study between the single façade case and the PDSF. The aforementioned studies propose a purely experimental approach essentially aimed at estimating the wind pressure on the inner skin of a PDSF. However, this kind of approach exhibits limitations if the net load on the permeable layer is to be measured, since it could be hard to position pressure sensors on that skin if the model's dimensions are small. In addition to this, a quantification of the expected flow rate through the permeable skin is not quantifiable or, at best, some spot measurements can be performed. In practice, cases exist in which this information could become of great relevance for addressing potential aero-acoustic problems that may arise when porous elements are exposed to wind [7], as the tonal noise emission is usually associated with a through velocity threshold.

These limitations can be overcome by a Computational Fluid Dynamic approach that is able to provide a continuous representation of velocity and pressure fields. Within the CFD framework, literature offers several studies focused on the fluid interaction of porous elements and they propose essentially two alternatives for modelling fluid interaction with porous elements [8]. The first one deals with explicit modelling of the geometry of the permeable element. However, this option is computationally unaffordable, especially if the porous element is part of a more complex system, as in the case of a PDSF. The other possibility is to rely on a porous-media approach by representing the porous element by means of a surface with zero-thickness or with a 3D volume, where a pressure jump or momentum source/sink term is used to account for the porosity effects. When the thin surface is used, the approach is usually referred to as a porous baffle: the porous element is modelled as a continuous surface in the computational domain and, at the cell faces of that surface, the pressure jump condition is realized by means of a resistance source in the Navier–Stokes momentum equation, as a function of the velocity component normal to the surface itself. Xu et al. [9] discussed the performances of the pressure jump approach on a perforated rectangular cylinder, and concluded that, if compared to explicit modelling, some local discrepancies exist but good agreement is found for the mean pressure and velocity fields. A porous baffle model is also used in many other application fields, such as modelling the air flow through perforated tiles at data centres [10], or simulating the presence of actuator disks [11] to mention a few. The main limitation of the pressure jump approach is that its validity holds for thin structures only. When more complex porous structures are to be considered (i.e., with anisotropic characteristics), the so-called porous media approach is more suitable than the porous baffles one. It consists of representing the porous elements by means of a 3D volume in the computational domain, where the momentum resistance is applied to the cells of that volume. This approach was used by Feichtner et al. [12,13] to model the wave interaction with perforated sheets and cylinders. Given that the PDSF may be formed with different types of outer skin, including louvres, perforated or expanded metal and wire meshes, the porous media approach will be considered here to be the most appropriate tool for achieving numerical modelling of the porous façade.

This paper proposes a new methodology for addressing the design of a PDSF in terms of the wind effects: experimental tests and CFD simulations with porous media models will play complementary roles, to address the computation of the design pressures on both façade layers and to estimate the flow rate through the permeable skin.

This method is presented in the form of a case study, namely the *ENI Head Office* building complex.

### *The Case Study*

The *ENI Head Office* case study is a building complex made up of three interconnected buildings, as shown in Figure 1. The complex covers 65,000 m<sup>2</sup> and the height of the structures reaches 45 m. The buildings are designed with a permeable double skin façade system: the inner glazed skin is covered by perforated metal in such a way that a gap flow can develop in the cavity between the two skins. Specifically, the ICO and SKG buildings are covered by a so-called Orange Skin, made up of stainless steel perforated metal with circular holes 6 mm in diameter, spaced 8 mm apart (porosity equal to 50%). The ICO and the LMK buildings are connected by a bridge, that has only the Orange Skin with no inner façade as cladding. Lastly, the LMK building's porous layer is characterized by the Blue Skin, horizontal louvres made up of metal sheets perforated by circular holes 6.35 mm in diameter, spaced 8 mm apart (porosity equal to 55%).



**Figure 1.** Render of the ENI Head Office in Milan.

Since the outer skin is made up of perforated metal sheets, air passing through the holes can generate undesired tonal noise [14].

There are two main problems to be addressed for this case study: the definition of the wind-induced pressure on both layers of the cladding system, and the estimation of the flow rate expected across the porous skin. The latter can subsequently be combined with a wind climate study of the buildings' area, in order to quantify the risk of exceeding of the threshold velocity associated with tonal noise emission by the perforated metal sheets.

## **2. Methodology**

Addressing the assessment of wind effects on a permeable double skin façade implies facing a typical multi-scale problem. The relevant effects due to immersion of the building in the Atmospheric Boundary Layer must be considered together with the local phenomena that develop at the level of the porous façade's openings. Local flow will be characterized by scales expected to have dimensions comparable to those of the openings themselves (usually in the order of cm), and will be affected by the boundary layer that develops locally.

An experimental-based approach, typically consisting of wind tunnel tests on a rigid scale model, is one of the most commonly adopted tools for addressing estimation of cladding loads on buildings. However, when dealing with a PDSE, reproducing the porous layer properly in the scale model may represent an issue, given the already small (at

full scale) dimensions of the façade's details. This is particularly concerning when the geometry of the permeable layer is characterized by a 3D geometry that will induce flow deflection. Additionally, as previously pointed out, quantification of the expected flow rate through the PDSF, that may be relevant for design purposes, is hard to assess using a purely experimental approach. These limitations make it necessary to consider a CFD model as a complementary tool for addressing the wind interaction issue for the PDSF. Within the numerical framework, the porous media approach can be applied to reproduce the effects due to the porous façade without explicitly modelling it in the computational domain, as already introduced in Section 1.

A new methodology based on a combined experimental-numerical approach is proposed and the two methods play complementary roles. Specifically, the experimental part consists of wind tunnel tests on a rigid scale model, where the porous façade is reproduced physically, essentially aimed at estimating the cladding loads for the PDSF. The numerical part, on the other hand, is based on a dedicated CFD model, referred to here as the *CFD reduced order model*, able to model the PDSF, thereby overcoming the multi-scale nature of the problem. The latter will address estimation of the flow rate through the porous layer, after it has been validated against experimental data.

The methodology, based on experimental tests and numerical simulations, was specifically designed to allow a quantitative approach to assessing the wind effects for the porous double skin façade. It is essentially made up the following steps:

1. Aerodynamic characterization of the porous elements by means of the pressure loss coefficient.
2. Wind tunnel tests on a rigid scale model of the building complex, on which the double skin cladding system is reproduced.
3. Computation Fluid Dynamics simulations, where a dedicated reduced-order model is used to include the effects due to the PDSF.

### 2.1. First Stage—Aerodynamic Characterization of the Porous Layer

When dealing with porous elements, their loading condition due to wind is mainly affected by their resistance to the flow, which depends on the pattern of the openings and the wind attack angle [15]. When the air flows through a porous element, there is an interaction between the fluid and the structural elements which is related to the aerodynamic properties of the medium and the characteristics of the fluid. A pressure drop in the fluid occurs when the flow passes through the permeable element. The pressure loss coefficient  $k$ , that synthetically describes the resistance to through flow, is proportional to this pressure drop and is defined as:

$$k = \frac{\Delta p}{1/2\rho U^2} \quad (1)$$

where  $\Delta p$  is the pressure drop between the windward and the leeward side of the porous screen,  $\rho$  is the air density and  $U$  is the mean wind speed. According to the state of the art, the pressure loss coefficient can be used to synthetically describe the aerodynamic behaviour of porous elements, especially when they are characterized by planar geometries, like perforated metals or wire meshes.

Within this case study, the pressure loss coefficient  $k$  is measured experimentally in an open-circuit wind tunnel. A schematic representation is shown in Figure 2: the porous screen is placed in the measurement section, orthogonally to the incoming flow. Two Pitot tubes, upstream and downstream, are used to measure the pressure drop.



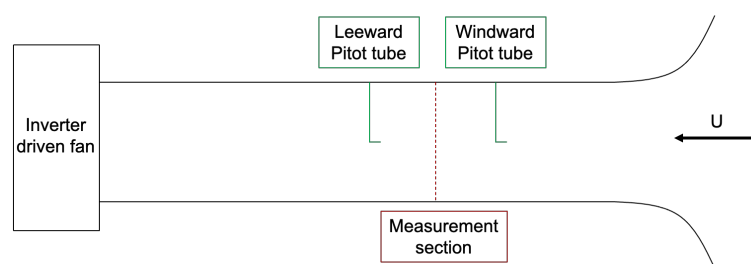


**Figure 2.** Experimental setup to measure the pressure loss coefficient.

## 2.2. Second Stage—Wind Tunnel Tests

The experimental part of the proposed methodology consists of wind tunnel tests on rigid scale models. From this stage, cladding loads on the PDSF can be assessed and data for subsequent validation of the CFD model is provided. Below, the experimental setup and model are described in relation to the *ENI Head Office* case study.

Wind tunnel tests were done at the Politecnico di Milano Wind Tunnel, a 1.5 MW closed circuit wind tunnel. The boundary layer test section was 4 m high, 14 m wide and 36 m long. The large dimension of the test section makes it possible to adopt a large geometric scale  $\lambda_L$  ( $\lambda_L = \text{model}/\text{real}$ ) with low blockage ratio, equal to 3% for this test. The geometric scale is chosen to be 1:75 thereby guaranteeing a gap between the two skins large enough to let the gap flow develop (equal to 2 cm on the scale model); geometric scaling was applied to the overall structure excluding the porous elements. For these elements, the kinematic similitude of the flow condition between the full and model scales is ensured by means of the pressure loss coefficient  $k$ , that must be maintained [5]. Hence, the same perforated metals as in the full scale case are used in the model, as the hole diameters are compatible with the overall model's dimensions.

The wind speed for the tests is 8.90 m/s in the experimental tests, that implies a velocity scale  $\lambda_V$  equal to 1:3.09, assuming a full scale reference wind speed of 27.5 m/s. The time scale  $\lambda_T$ , equal to the ratio between the length and velocity scales, is equal to 1:24.3. Table 1 summarizes the reference lengths and velocities as well as the sampling time and frequency at model and full scale. The reference velocity for the tests was measured by a Pitot Tube placed 7 m upstream of the model, 0.60 m above the ground.

**Table 1.** Reference height, velocity, sampling time and frequency for the wind tunnel tests.

	Model Scale	Full Scale
$H_{ref}$	0.60m	45 m
$U@H_{ref}$	8.90 m/s	27.5 m/s
Sampling time	180 s	4370 s
Sampling frequency	500 Hz	20.6 Hz

### 2.2.1. Model Description and Instrumentation

The buildings in the test section are shown in Figure 3. The model was fitted with 400 pressure taps: of these, 198 were distributed on the inner sealed façade and the remaining 202 were used to measure the differential net pressure on the porous layer. The large scale of the model made it possible to position sensors on the porous layer, in an attempt to minimize the distortions due to the presence of the tubes with the gap between the two façades: Figure 4 shows a detailed view of how the pressure taps were arranged on the model's surface. Pressure measurements were taken using high-speed Initium pressure scanning equipment (with a sampling frequency equal to 500 Hz) and miniature pressure scanners PSI ESP-32 HD, each of which have 32 pressure channels.

Figure 5 shows the wind directions convention adopted in the wind tunnel tests: 36 exposures, at 10° spacing, were considered.



Figure 3. Wind tunnel tests on 1:75 scaled model of the ENI Head Office buildings.

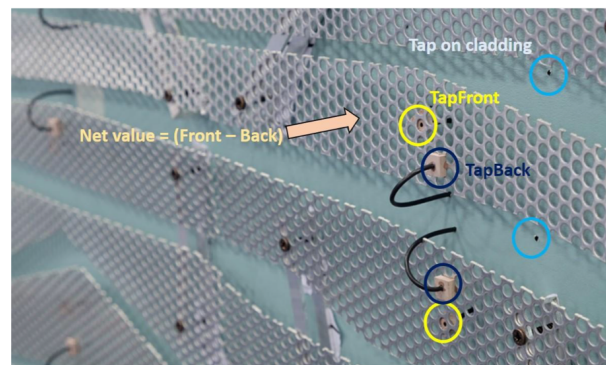


Figure 4. Pressure taps on the model surface: detail on the set up for measurement of the differential pressure on the porous layer.

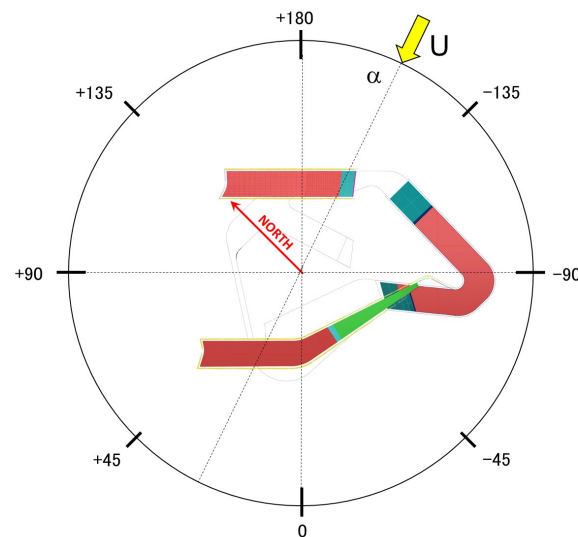
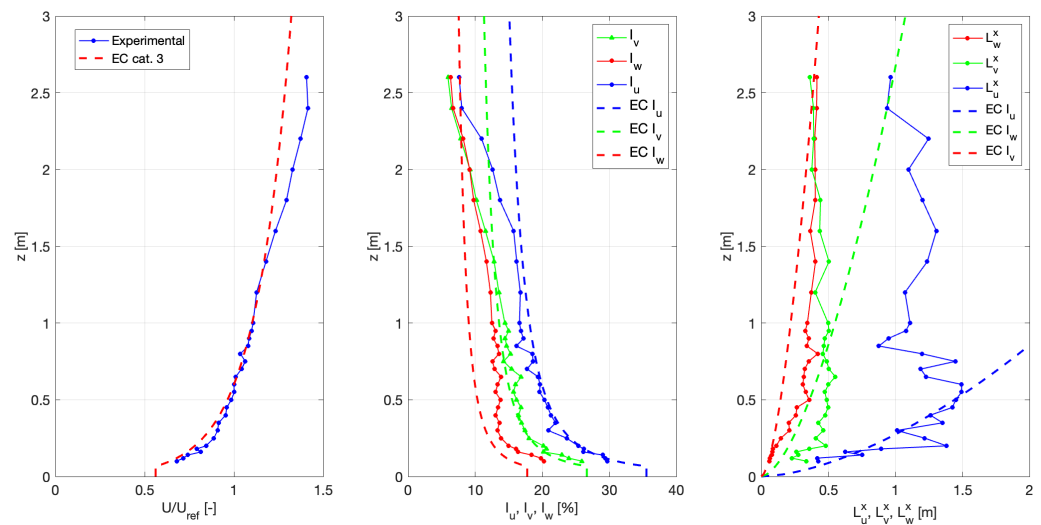


Figure 5. Wind direction convention. Red arrow shows the true North direction.

Multi-hole cobra probes were used to measure the three-components of the velocity vector in the gap in the PDSF. These sensors were installed in the gap between the perforated metal and the inner skin as well as in front of the external side of the porous façade. To achieve a reliable estimation of the gap flow, cobra probes were mounted pointing towards the expected direction of the flow.

### 2.2.2. Flow Configuration

Passive turbulence generators together with roughness elements were used to generate a representative wind field for the case at hand. Figure 6 shows the mean velocity (left), turbulence intensities (centre) and integral length scales (right), measured at the centre of the turntable, compared to those proposed by Eurocode, category III, assumed as a target. The  $z$  coordinate used in the plots is in model scale. The mean velocity profile is normalized in relation to the reference velocity  $U@H_{ref}$ , where  $H_{ref}$  is the maximum building height. Profiles compare well with the target ones, especially when focusing on  $z$  lower than 1 m. Lastly, Figure 7 shows the streamwise velocity spectrum, measured at a height of 1 m. It was normalized by the measured integral length scale and showed good agreement with both the Von-Karman and the Eurocode spectra.



**Figure 6.** Wind profiles used for the wind tunnel tests. **Left:** mean speed profile. **Centre:** Turbulence intensities. **Right:** Integral length scales.

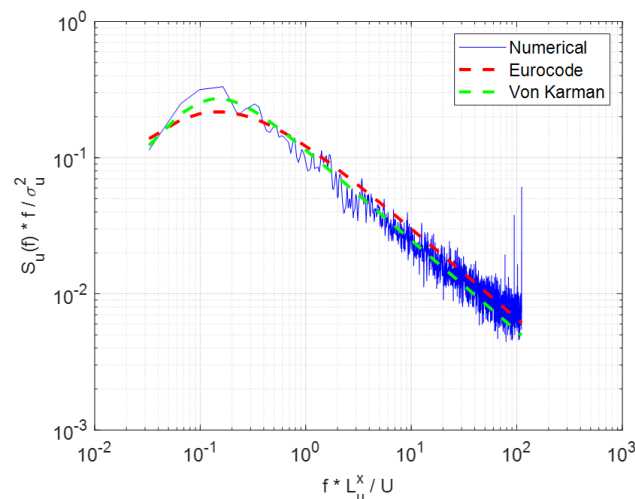


**Figure 7.** Streamwise velocity spectrum at 1 m height compared to the Von-Karman spectrum and to the Eurocode one.

### 2.3. CFD Reduced Order Model of the PDSF

To estimate the velocity flow field and to quantify the flow rate across the porous façade, a dedicated Computational Fluid Dynamic model was developed. It relies on a porous media model and will be referred to as *reduced order model*, as it is able to avoid explicit modelling of the porous geometry, thereby reducing the computational complexity

of the numerical simulations. It is based on the Darcy-Forchheimer model for porous media: the porous façade of the PDSF is not explicitly modelled in the computational domain, but it is reproduced by means of a “porous” slab and for each cell in that volume, a momentum resistance term is applied according to the Darcy-Forchheimer model [16]. Figure 8 presents a schematic view of how the PDSF is modelled in the computational domain: the external porous façade in the physical system corresponds to a special set of cells in the computational domain, responsible for the momentum defect.

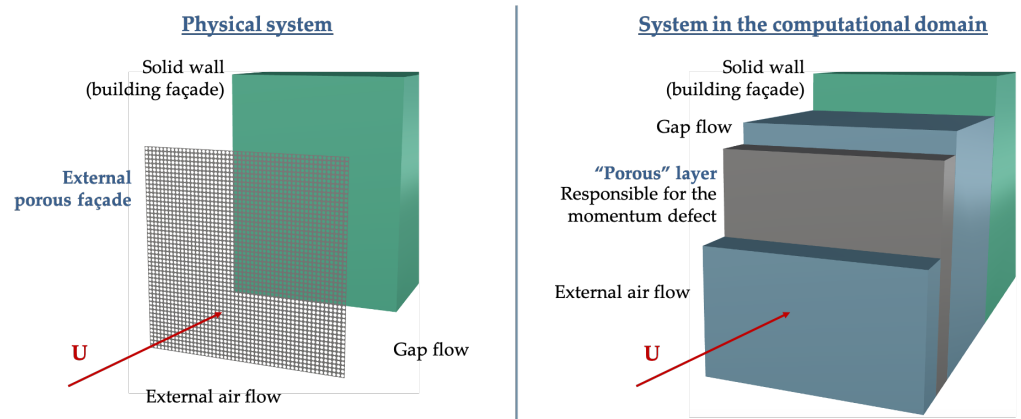


**Figure 8.** Schematic view of the reduced order modelling of the porous layer: comparison between the physical system (left) with the PDSF system in the computational domain (right).

Since a steady-state approach was considered, the equations solved for the incompressible flow were:

$$\begin{aligned} \rho(\mathbf{U} \cdot \nabla)\mathbf{U} - \mu\Delta\mathbf{U} + \nabla p &= \mathbf{S}_m \\ \nabla \cdot \mathbf{U} &= 0, \end{aligned} \tag{2}$$

where  $\mathbf{U}$  is the velocity vector,  $\rho$  the fluid density,  $\mu$  the dynamic viscosity and  $p$  the pressure. The momentum sink term  $\mathbf{S}_m$  for modelling the porosity effects is written as:

$$\mathbf{S}_m = -\left(\mu\mathbf{D} + \frac{1}{2}\rho|\mathbf{U}|\mathbf{F}\right)\mathbf{U}, \tag{3}$$

where  $\mathbf{D}$  represents the porosity effects proportional to viscosity and  $\mathbf{F}$  accounts for the total pressure loss proportional to the incoming flow’s dynamic pressure. The dimensions are  $[\mathbf{D}] = \frac{1}{m^2}$  and  $[\mathbf{F}] = \frac{1}{m}$  respectively. The source term  $\mathbf{S}_m$ , which has a force per unit volume dimension or, equivalently, a pressure gradient dimension, will be responsible for the actual pressure gradient through the porous slab, associated with the cross-flow. As the porous elements considered here are characterized by a low viscosity level and high pressure contribution, the proposed model focuses on the pressure intake (tensor  $\mathbf{F}$ ), neglecting the viscous supply, represented by  $\mathbf{D}$ .

According to the state of the art, the perforated metal sheets represent the simplest case, as the momentum sink term is computed by means of a diagonal tensor with only one term different from zero, i.e., the one associated with the flow component orthogonal to the porous slab. This assumption implies assuming that the other velocity components make no contribution to the source term  $\mathbf{S}_m$  and so, neglecting any flow deflection due to the permeable layer, which is expected to be of no relevance in the case of perforated metals. Hence, assuming a Cartesian reference system in which the porous slab is lying in the  $y - z$  plane, Equation (3) becomes:

$$\begin{bmatrix} S_{m,x} \\ S_{m,y} \\ S_{m,z} \end{bmatrix} = -\frac{1}{2}\rho|\mathbf{U}|\mathbf{F} \begin{bmatrix} 1 & 0 & 0 \\ 0 & 0 & 0 \\ 0 & 0 & 0 \end{bmatrix} \begin{bmatrix} U_x \\ U_y \\ U_z \end{bmatrix} \tag{4}$$



where the  $F$  coefficient is computed as the pressure loss coefficient  $k$  (experimentally computed) divided by the thickness of the *porous slab* in the computational domain.

The numerical solver used for this analysis is the open-source software, OpenFOAM: the flow is calculated by means of a finite volume approach, solving the steady-state incompressible Reynolds-Averaged Navier-Stokes (RANS) equations, using adapted turbulence modelling to achieve closure and suitable boundary conditions, as will be detailed in the next sections.

### 2.3.1. CFD Mesh

The building's geometry is reproduced in the computational domain, assuming a length scale of 1:75, hence with a maximum height of 0.60 m. The mesh was formed within a domain  $14\text{ m} \times 15\text{ m} \times 6.5\text{ m}$ , as sketched in Figure 9. The mesh is realized by means of a top-bottom strategy, using the OpenFOAM mesh generator, SnappyHexMesh. A background mesh is formed using a structured grid 0.5 m in size, then a successive refinement in the porous slabs area is performed, up to a final mesh size on the porous surface of  $4 \times 10^{-3}\text{ m}$  with a total number of 8.7 million cells. To check the quality of the mesh and the refinement level, the *yPlus* parameter was calculated and checked to be higher than 30 to allow the application of the wall functions. Figures 10 and 11 show a detailed view of the mesh: the former shows an horizontal section of the computational domain, the latter focuses on the porous slab representing the perforated metal sheets for the SKG building.

Each numerical simulation is run on an HPC facility using 3 nodes with 8 cores each.

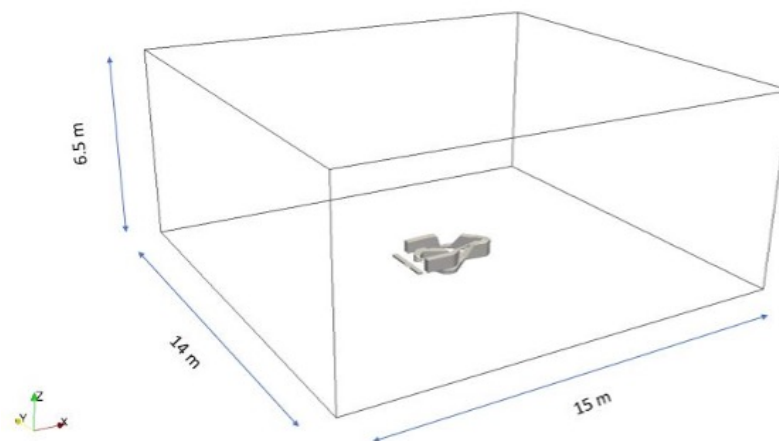


Figure 9. Geometry of the overall domain and related dimensions.

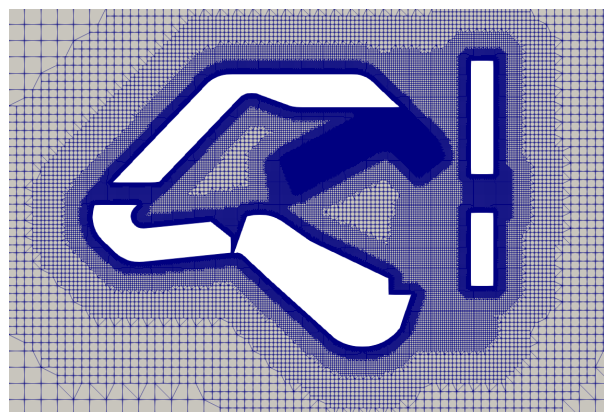


Figure 10. Mesh buildings.

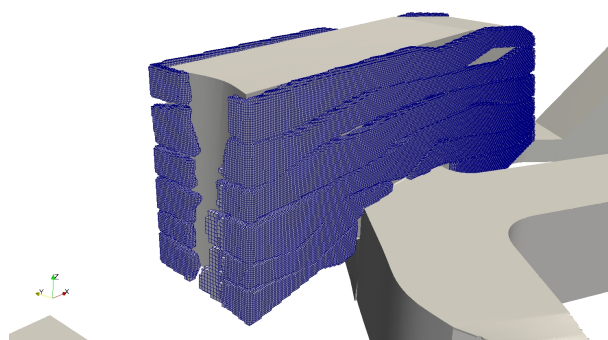


Figure 11. Mesh porosity.

### 2.3.2. Numerical Setup and Boundary Conditions

The numerical model is a steady state incompressible RANS standard, with a  $k - \epsilon$  turbulence model, that is suitable for modelling the atmospheric boundary layer and flow around buildings [17]. All the schemes were selected as second order, upwind-biased and a SIMPLE algorithm was used for the pressure-velocity coupling. The atmospheric wind profile corresponding to the wind tunnel testing profile was imposed at the inlet.

Boundary conditions are defined as follows:

- INLET: **atmBoundaryLayer** with reference wind speed  $U = 10$  m/s and specified wind direction, **zeroGradient** for pressure
- OUTLET: **InletOutlet** for velocity, **fixedValue** pressure  $p = 0$
- SOLID WALL: zero velocity with standard wall functions
- BACK and FRONT:  $U$  symmetry,  $p$  symmetry.

Simulations were run for 24 different wind directions, i.e., from  $0^\circ$  to  $360^\circ$ , at  $15^\circ$  intervals, in relation to the convection shown in Figure 5. Figure 12 describes the boundary conditions in the case of the incoming wind direction being equal to  $+90^\circ$ .

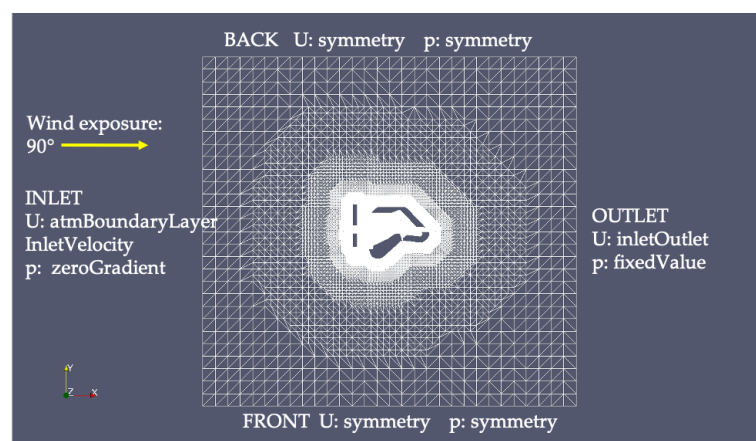


Figure 12. Boundary conditions.

## 3. Results

### 3.1. Pressure Loss Coefficient

The pressure loss coefficient  $k$  was measured for both the porous façades, i.e., the Orange and the Blue skin. The  $K$  coefficient was computed for different inlet velocities to ensure Reynolds independence. Figure 13 shows the pressure loss coefficient for both the porous layers, for varying incident wind speeds. The Orange Skin, characterized by a smaller porosity value, presented a slightly higher  $k$  coefficient than the Blue Skin. Both of them exhibited a stable  $k$  value in the tested range of velocities. From this point on it was assumed that the Orange and the Blue Skins were characterized by  $k = 2.5$  and  $k = 1.9$

respectively. These values were then used as scaling parameters for the porous façade in the WT model and as input data in the Darcy-Forchheimer CFD model.

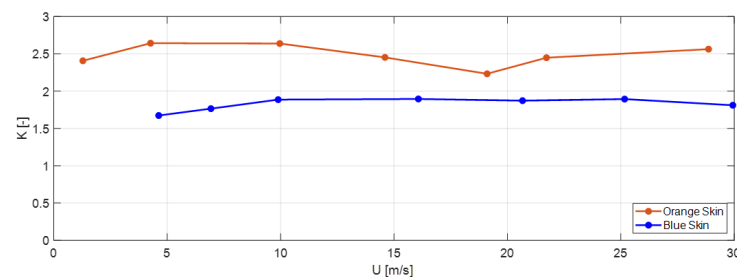


**Figure 13.** Pressure loss coefficient for the Orange and Blue Skins.

### 3.2. Experimental Results

The wind tunnel tests results are presented in this paragraph. The goal for this phase was to assess the wind-induced pressure on both layers the cladding system is made up of.

The pressure data acquired in the wind tunnel tests was expressed in a non-dimensional form, as the local pressure coefficient, defined for a generic pressure tap  $k$  as:

$$C_p^k(t) = \frac{p^k(t) - p_0}{q_H}, \quad (5)$$

where  $p^k(t)$  is the local pressure,  $p_0$  the reference static pressure in the test section and  $q_H = 1/2\rho U_{ref}^2$  the wind's reference dynamic pressure at  $H_{ref} = 45$  m. The (5) indicates that positive  $C_p$  represents thrusts and negative pressure indicates suctions. When the pressure data is referred to the porous layer, the net wind pressure is computed as the difference in the time domain between the external and internal pressure coefficients, acquired by the  $k$ -th tap:

$$C_{p,net}^k(t) = C_{p,ext}^k(t) - C_{p,int}^k(t). \quad (6)$$

The pressure data is presented in the sections that follow: specifically, the analysis focused first on the comparison of time histories between pressure taps on the porous skin and on the glass façade. Then, envelope maps of peak values, useful for cladding design purposes, are presented.

#### 3.2.1. Time Histories Comparison

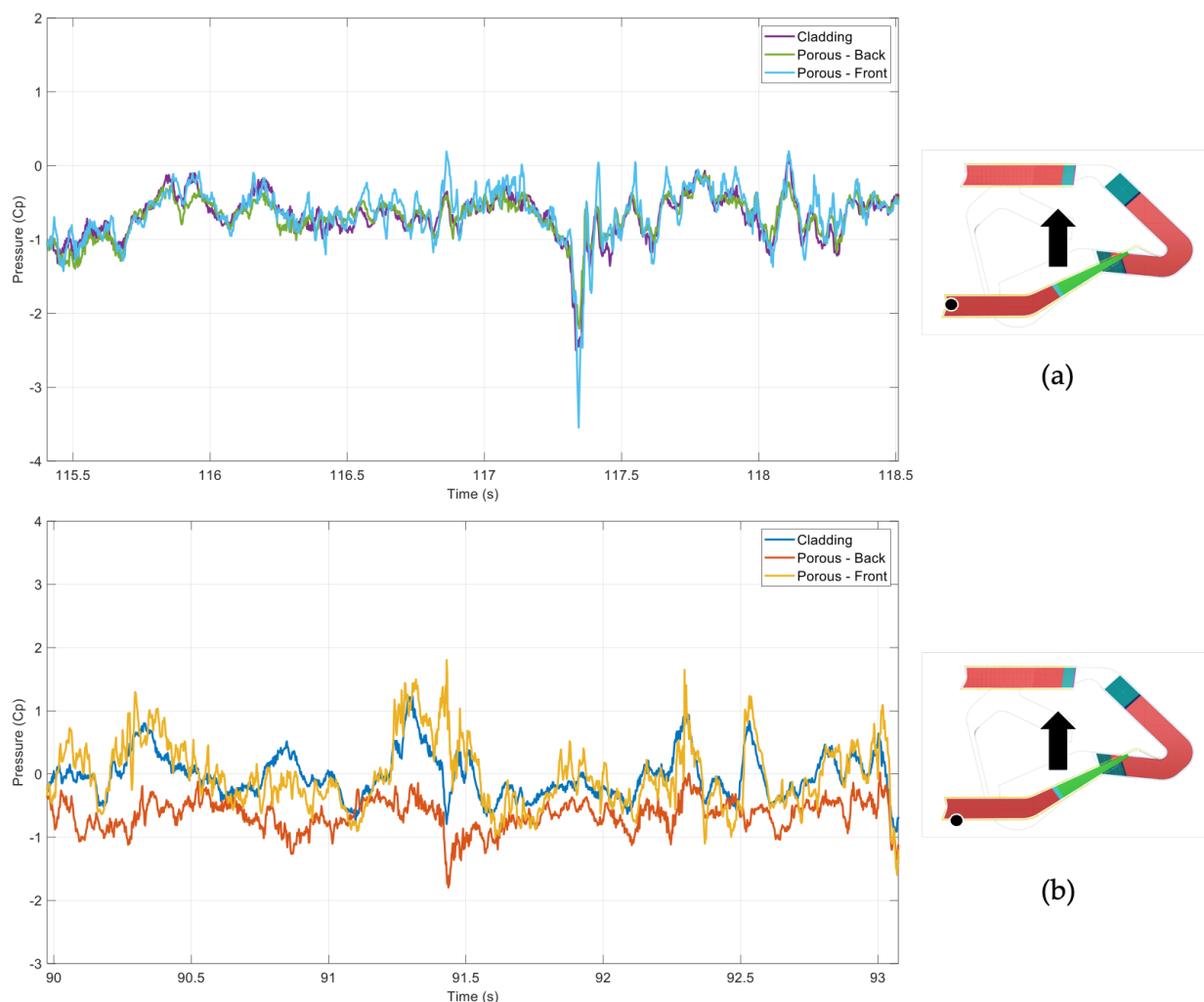
This section presents a comparison of the simultaneous pressure time histories acquired on the permeable double skin façade during the wind tunnel tests. Different positions are analysed: upwind and downwind corners, along with the bridge locations, where the cladding is made up of the perforated metal only.

Figure 14 shows two snapshots extrapolated from simultaneous pressure measurements on the porous skin and the corresponding position on the inner façade. The wind direction is  $0^\circ$ , as specified by the arrow in the left plots in Figure 14. Taps placed close to the ICO building corners were selected, as these are the spots mainly affected by the highest gap flow.

Figure 14a focuses on the corner at the separation bubble and presents the time histories of 3 different pressure taps: one was placed on the inner façade and the others record pressure on the porous skin (front and back, according to the same convention as Figure 4). The signals showed a very high correlation and they shared the same evolution over time. The blue line, associated with the front tap on the porous layer, is characterized by sharper peaks compared to the green (back tap on the porous skin) and purple (inner façade) lines. Table 2 summarizes the mean value, standard deviation and peak values for the signals, along with the net signal, computed according to Equation (6). The first three were characterized by the same negative mean value, while higher standard deviation was found for the front tap. Table 2 also shows the peak pressure coefficients associated with a

22% probability of exceeding [18]. The most negative peak value ( $\check{C}_p$ ) was for the front tap, i.e.,  $-2.87$ , and it decreased to  $-2.51$  for the tap on the inner façade.

Figure 14b shows the corresponding three signals when moving to the upwind side of the same ICO corner. When focusing on the porous skin signals, the yellow (front) and the red (back) lines present a lower correlation than the front-cladding couple. The cladding signal is very close to the yellow line (front tap on the porous façade), even though it does not present the sharpest peaks anymore: the presence of the porous skin is reflected in the characteristics of the time histories, as the one recorded by the inner façade tap is smoother than the yellow line. Table 2 reports some statistics for these signals: the front tap on the porous skin is characterized by the highest standard deviation (0.51) and the highest positive peak  $\check{C}_p$  (2.42). The table also shows some statistics for the net signal, obtained as the difference between the front and back time histories.



**Figure 14.** Time domain comparison between the glass façade and the porous skin pressure signals: the plots on the left show a snapshot of the signals, while those on the right show the location of the pressure taps along with the incoming flow direction. (a) Downwind side. (b) Upwind side.



**Table 2.** Pressure taps statistics, wind direction 0°.

	Location	Mean $C_p$	Std	$\hat{C}_p / \check{C}_p$
Negative peak	Glass façade	−0.65	0.26	−2.51
	Porous, front	−0.61	0.30	−2.87
	Porous, back	−0.65	0.22	−2.19
	Porous, net	0.05	0.18	−1.22
Positive peak	Glass façade	0.01	0.39	1.82
	Porous, front	−0.02	0.51	2.42
	Porous, back	−0.64	0.23	−1.93
	Porous, net	0.62	0.53	3.45

Figure 15 shows a 3 s (model scale) snapshot of the bridge’s pressure signals, when the incoming wind direction is  $-30^\circ$ , as described by the black arrow. The red (front) and the blue (back) time histories present a negative correlation, as there is an increase in the first corresponding to a decrease in the others. The cross-correlation, normalized by the product of the standard deviations, is  $-0.74$ . The net pressure, described by the green line, results in an amplification of the peaks, in relation to the front values, as it is computed as the difference between the front and back. This also highlights the presence of a certain flow rate through the permeable layer. Table 3 summarizes the mean value, standard deviation and peak value of the 3 signals: the net pressure reaches  $4.86 C_p$  for a wind direction of  $-30^\circ$ .

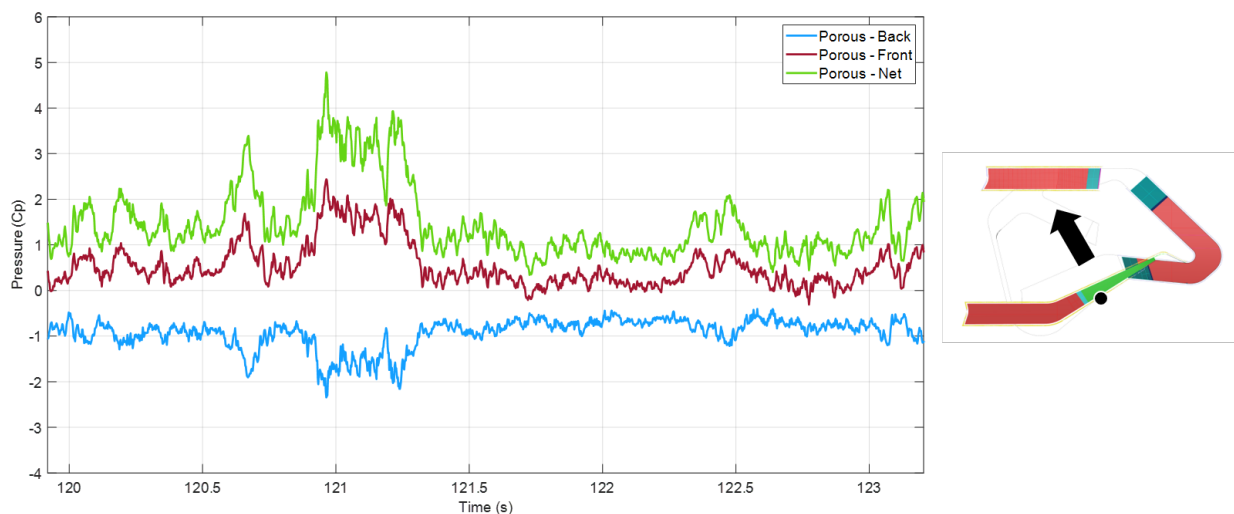


**Figure 15.** Time domain comparison between the pressure signals acquired by the pressure taps on the bridge: the plot on the left plot shows a snapshot of the time histories, while plot on the right shows the location of the pressure taps along with the incoming flow direction.

**Table 3.** Pressure taps statistics, wind direction  $-30^\circ$ .

	Location	Mean $C_p$	Std	$\hat{C}_p / \check{C}_p$
Bridge	Porous, front	0.50	0.36	2.35
	Porous, back	−0.94	0.26	−2.62
	Porous, net	1.445	0.58	4.86

### 3.2.2. Velocity Measurements

To characterize the gap flow between the two skins, for the most significant exposure angles and at some spots (i.e., bridge and building corners), Cobra Probes were used to measure the velocity locally.

The cobra probes were positioned in the locations in which the highest flow across the porous medium is expected, i.e., the bridge between the LMK and ICO buildings (where there is only the porous layer, without the inner cladding) and on the ICO building's upper corner. All the locations are sketched in Figure 16. The exposure angle is  $-30^\circ$  for the bridge (flow orthogonal to the bridge mesh) and  $0^\circ$  for the ICO corner, as depicted in Figure 16. Table 4 summarizes the results for the ICO building corner and the bridge respectively:  $V/V_{ref}$  indicates the ratio between the magnitude of the velocity vector measured by the Cobra Probes and the undisturbed flow velocity, measured by the Pitot tube.

When the flow is orthogonal to the bridge ( $-30^\circ$ ), the latter is subjected to the highest flow rates, leading to local velocities in the order of 70–80% of the reference velocity. These values were used to validate the CFD results by comparing the velocity fields.

**Table 4.** Velocity measures.

Position	$H/H_{ref}$	Wind dir.	$V/V_{ref}$
A	0.95	$0^\circ$	0.65
B	0.85	$0^\circ$	0.70
C	0.95	$0^\circ$	0.70
D	0.95	$0^\circ$	0.68
E	0.85	$-30^\circ$	0.92
E	0.65	$-30^\circ$	0.89
F	0.85	$-30^\circ$	0.70
F	0.65	$-30^\circ$	0.83
G	0.85	$-30^\circ$	0.57
G	0.65	$-30^\circ$	0.87
H	0.85	$-30^\circ$	0.48
H	0.65	$-30^\circ$	0.51

### 3.2.3. Design Values—Envelope Maps

One of the final purposes of the wind tunnels tests on the ENI Head Office is to assess the design cladding load. The design value for a cladding element is theoretically representative of the maximum correlated pressure over the surface of the panels the cladding is made up of. However, during the wind tunnel tests, pressure time histories were acquired at specific points (the locations of the pressure taps) that were usually characterized by a spatial resolution that does not allow direct estimation of the correlated pressure on that panel. So the single point pressure measurements acquired during experimental tests must become representative of the mean loading condition on a certain area. To do this, signals are post processed to remove small-scale contributions that do not significantly affect the total load on cladding elements. The most commonly adopted technique for removing these contributions relies on low pass filters in the time/frequency domain with a cut-off frequency (or an equivalent duration), computed according to the TVL theory [19]. It assumes a proportionality between duration and spatial extension of the pressure phenomena and proposes applying a time-domain filter to single point measurements to make them representative of a certain area. Specifically, the time domain filter is a moving average filter [20], where the time span is computed as:

$$\tau = \frac{K \cdot L}{V}, \quad (7)$$

where  $K$  is a constant equal to 4.5 [21],  $\tau$  is the averaging time,  $L$  is the diagonal of the reference area and  $V$  is the reference wind speed.

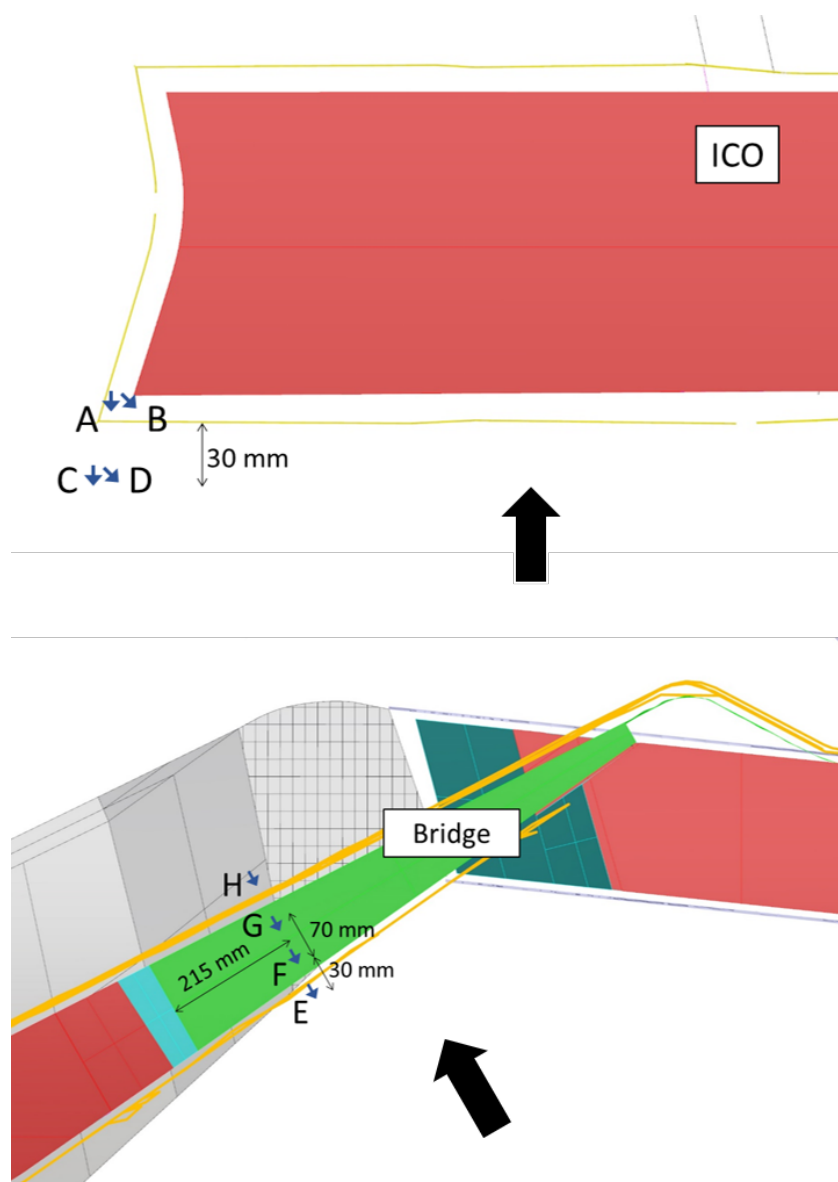


**Figure 16.** Cobra Position.

For the inner façade of the PDSF, a typical panel  $6 \text{ m}^2$  in size was considered, obtaining  $L = 3.4 \text{ m}$  (full-scale). As the reference full-scale velocity was equal to  $27.5 \text{ m/s}$ , the resulting  $\tau$  was  $0.56 \text{ s}$  full-scale. Conversely, for the perforated metal sheets, the reference area to be considered for the supporting structure was  $10 \text{ m}^2$ , leading to a slightly higher value of  $\tau$ , equal to  $0.73 \text{ s}$ . Hence, the signals acquired during the experimental tests were post-processed using a moving average filter for a time span equal to  $\tau$  computed by means of the TVL theory and referred to the scale model. Then, for each time history, peak values were calculated according to the Cook and Mayne method [18]: each time history of the pressure coefficient was divided into windows and the most positive/negative value was extracted from each window; a Gumbel distribution was fitted to the extreme values [22]. 10 windows of  $18 \text{ s}$  in size, equivalent to  $7.3 \text{ min}$  full scale, were used. The Gumbel distribution was then corrected according to the Cook and Mayne method [18], as the windows were shorter than the recommended  $10 \text{ min}$  full scale.

Then, the design values were computed as the most positive/negative peak pressure measured by each pressure tap for all wind directions. The upper and lower envelope maps, that encompass the most positive and negative (respectively) pressure experienced by each pressure tap, are presented below.

Figures 17 and 18 show the envelope maps of the positive and negative peak values respectively, measured on the inner façade of the PDSF system. Results are shown as 2D coloured maps where the in-plane development of the three buildings are shown. Areas close to the buildings' corners are affected by the strongest pressures and negative values are of a higher amplitude than the positive ones. As a matter of fact, as shown in Figure 18, the worst condition was reached with suction characterized by values up to  $-5C_p$ . Except for those regions, other portions of the inner façade were characterized by smaller peak values (in amplitude), in the order of  $-1.5--1 C_p$ .

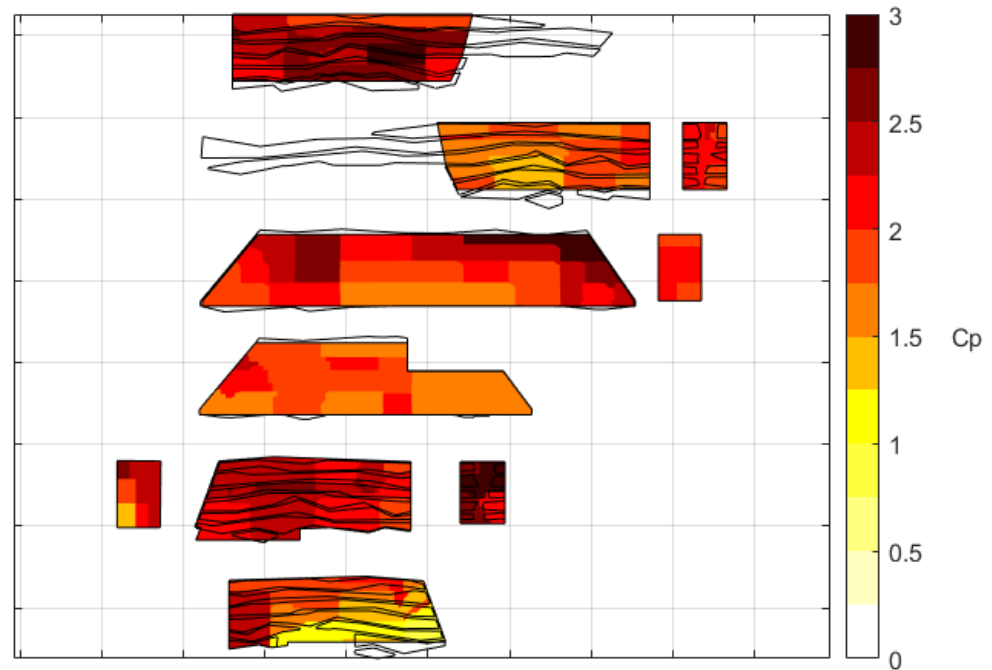


Figure 17. Envelope maps of the positive  $\hat{C}_p$ , measured on the inner façade of the PDSF.

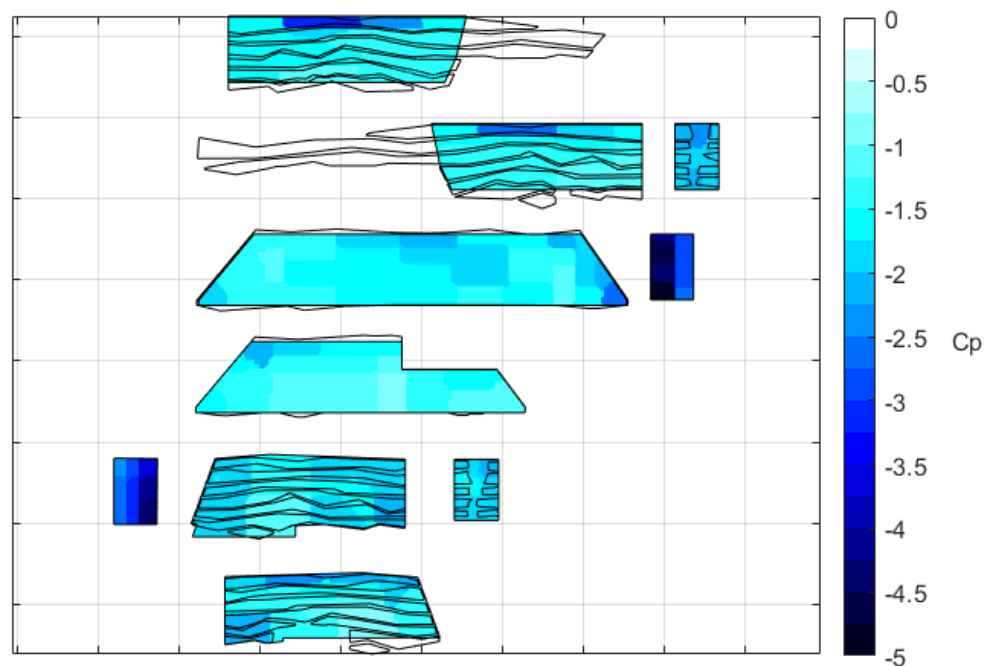


Figure 18. Envelope maps of the negative  $\check{C}_p$ , measured on the inner façade of the PDSF.



Switching to the permeable layer of the PDSF, Figures 19 and 20 show the upper and lower envelopes of the  $C_{p,net}$  measured on the perforated metal sheets. The Bridge is shown to be the portion affected by the highest thrusts (up to  $5 C_p$ ), while the SKG building's edge is affected by the most negative  $C_{ps}$ .

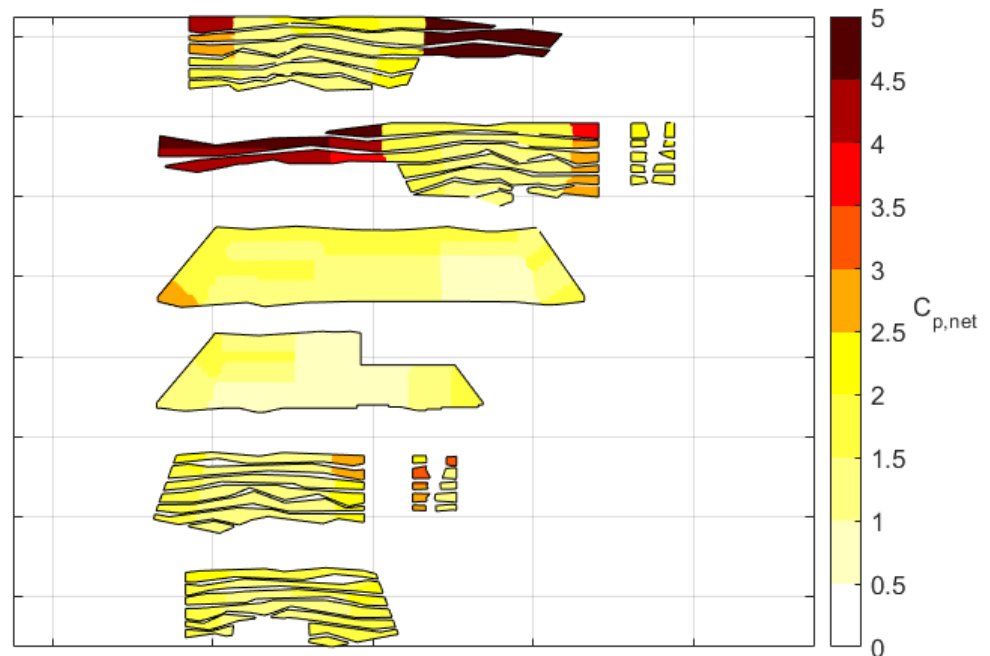


Figure 19. Envelope maps of the positive  $\hat{C}_{p,net}$ , measured on the porous façade of the PDSF.

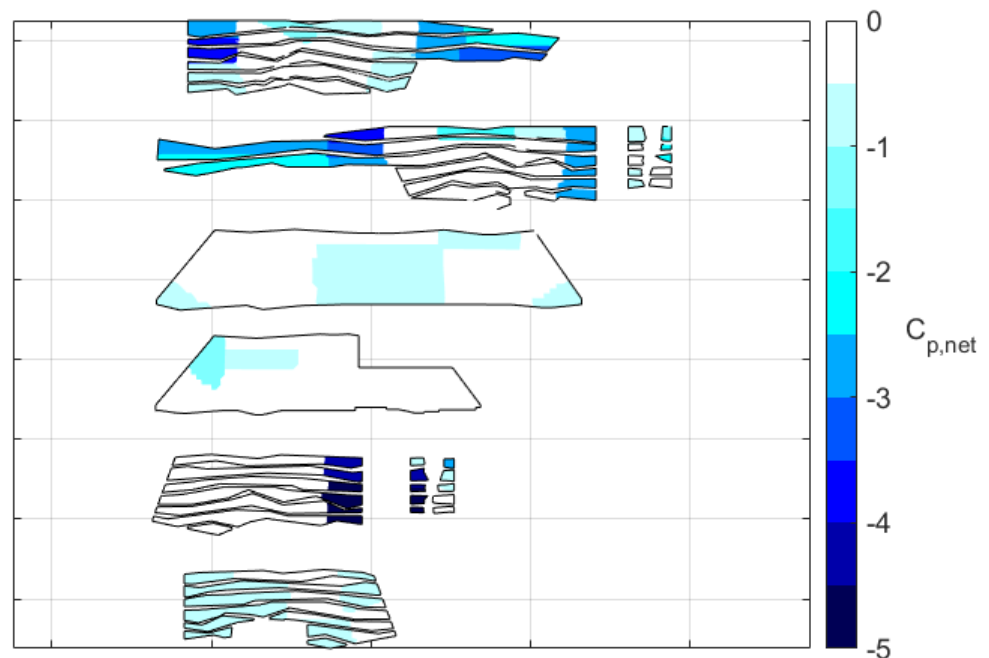


Figure 20. Envelope maps of the negative  $\check{C}_{p,net}$ , measured on the porous façade of the PDSF.

### 3.3. Numerical Results

This section presents the results obtained by CFD simulations, focusing first on one single wind direction and then providing a validation of the CFD model by comparing outputs with experimental data.

The flow field around the building was computed according to the setup presented in the Section 2.3. Results shown below focus on the  $-30^\circ$  wind direction, i.e., flow orthogonal

to the Bridge. The pressure distribution can be observed in Figure 21, sliced at a height of 0.5 m. Upwind regions are affected by positive pressure and a certain cross flow affects the Bridge area, given the pressure difference between the upwind and downwind sides. Figure 22 shows the streamlines for the same wind direction, highlighting the extension of the recirculation area behind the solid fences and the deviation of the flow.

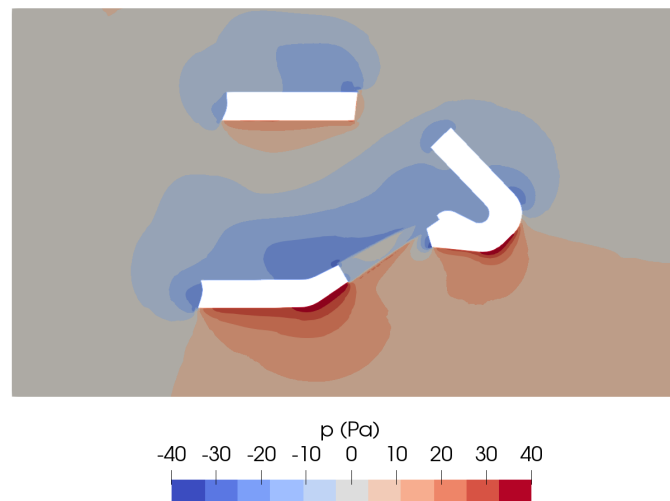


**Figure 21.** Pressure contour on ENI Head Office, at height 0.5 m model scale.

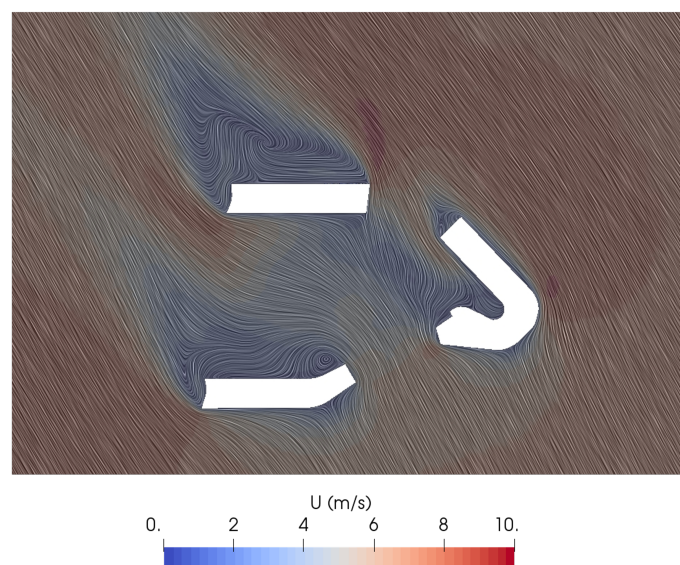


**Figure 22.** Velocity field on ENI Head Office, at height 0.5 m model scale.

The CFD analysis makes it possible to compute the expected crossing velocities through the porous façade. This is of utmost importance when assessing the potential risk of tonal noise emission, as it is usually associated with a threshold velocity. Hence, for the case at hand, the velocity field for the porous slab was obtained using the OpenFOAM cuttingPlane tool. This procedure was applied for each exposure angle, to calculate local mean through velocities in the mid plane of the porous slabs representing the perforated metal sheets. Crossing velocities were then normalized in relation to the reference wind speed, equal to 10 m/s. Results for a  $-30^\circ$  wind direction are shown in Figure 23. For this exposure, the areas affected by the highest flow rate are the Bridge and buildings' corners. The former is impacted by crossing velocities that are not negligible ( $V/V_{ref} = 0.7$ ) and this is mainly due to the fact that the cladding is made up of only the perforated metals in that region. Building corners are portions at which local velocities are in the order of 50–60% of

the reference value. This finding is in line with the experimental outputs, where the corner regions were found to be affected by the highest net pressure, indicating a certain flow rate through the permeable layer.

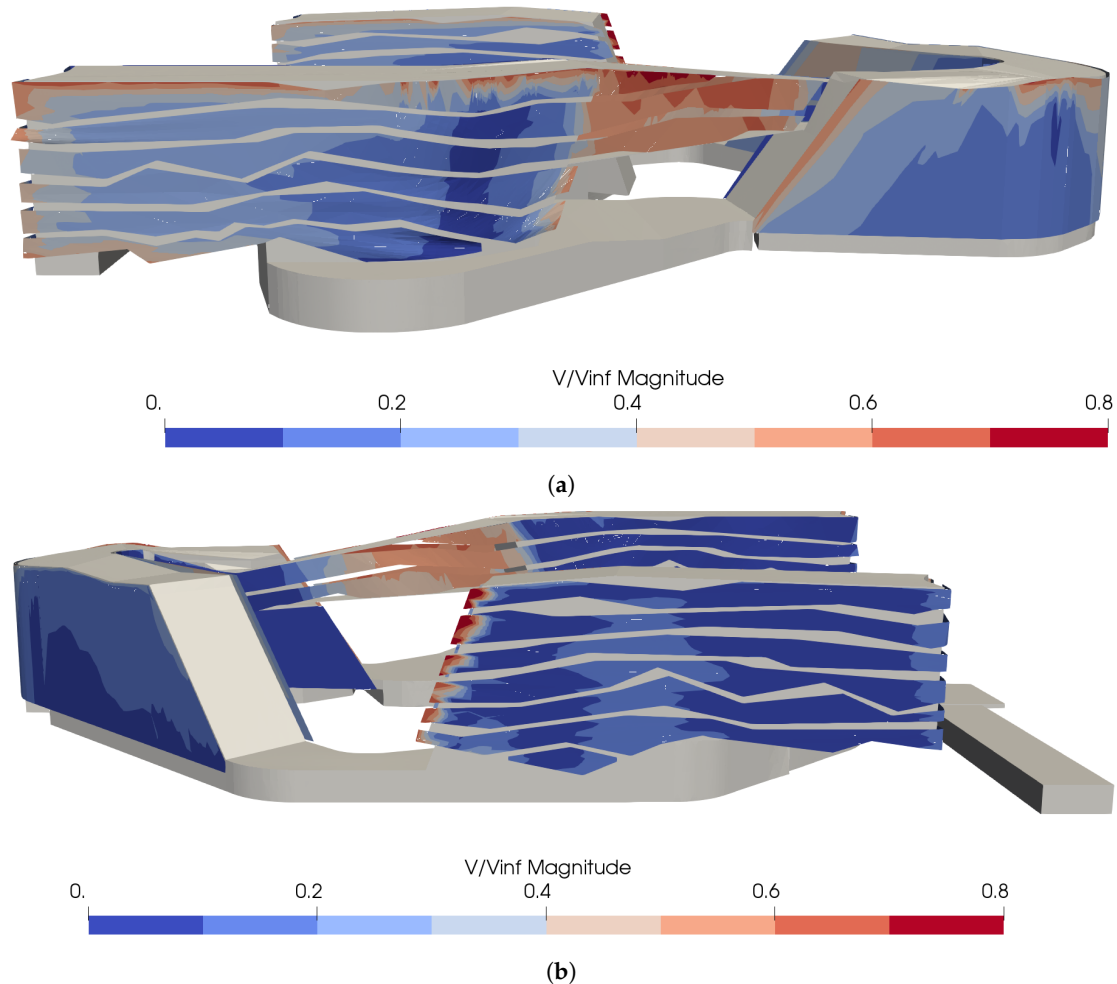


**Figure 23.** Mean crossing velocities measured in the midplane of the porous slabs, normalized in relation to the reference velocity. Wind direction  $-30^\circ$ . (a) Front view. (b) Rear view.

#### Validation of the CFD Reduced Order Model

The reliability of the numerical model strictly depends on validation using analytical or experimental data. For this case study, the CFD estimated crossing velocities were compared the spot velocity measurements from the wind tunnel tests to ensure the consistency of the results.

Specifically, the  $0^\circ$  and  $-30^\circ$  cases were considered. The results, summarized in Table 5, show good agreement even though the numerical model seems to slightly underestimate the velocity field.

**Table 5.** Velocity measures: WT vs. CFD.

Position	$H/H_{ref}$	$\alpha$	$(V/V_{ref})_{WT}$	$(V/V_{ref})_{CFD}$
A	0.95	0°	0.65	0.68
B	0.85	0°	0.70	0.66
E	0.85	−30°	0.92	0.79
E	0.65	−30°	0.89	0.59
H	0.85	−30°	0.48	0.52
H	0.65	−30°	0.51	0.54

Values were measured in the midplane of the porous “slab”; Positions are referred to the ones shown in Figure 16.

#### 4. Conclusions

The *ENI Head Office* case study represented an opportunity to develop and apply a new methodology for assessing the wind effects on a PDSF. The proposed method takes advantage of a combined numerical—experimental approach, where the former is dedicated to estimating the flow rate and the latter focuses on the assessing the cladding load. First, characterization of the aerodynamic properties of the perforated metal sheets, by means of the pressure loss coefficient, was carried out. Then, during the wind tunnel tests on rigid scale models, the pressure was measured on both layers of the PDSF: an analysis of the recorded time histories highlighted a strong correlation between upwind and downwind sides of the porous layer, especially in the Bridge area, qualitatively highlighting a certain flow rate through the porous façade. Then, quantification of the pressure load on the cladding was proposed by means of envelope pressure maps: for the inner façade, the strongest suction, up to  $-5C_p$ , are found close to the buildings’ edges while the porous layer is affected by  $5C_p$  thrusts in the area of the Bridge, where the façade presents only the perforated metal sheets. Additionally, spot velocity measurements were taken out on the wind tunnel scale model to quantify the flow rate through the perforated metal sheets, highlighting the presence of a non-negligible gap flow, with local velocities up to 70% of the reference value. A more detailed estimation of the flow rate through the porous layer was provided by the CFD reduced order model: a porous media approach was applied to overcome the multi-scale nature of the problem, making it possible to properly model buildings with a PDSF within the computational domain. According to the Darcy-Forchheimer model, a tensorial formulation was used to describe the momentum sink due to the permeable element. Specifically, the perforated metal sheets were treated as isotropic material with diagonal terms of the inertial tensor proportional to the experimentally computed pressure loss coefficient. Results from the CFD reduced order model compare well to the experimental velocities measures, showing that building edges and the Bridge are the areas most affected by the highest flow rate. Combining the numerical estimation of the through velocities with a local wind climate analysis, makes it possible to quantify the risk of exceeding the threshold velocity associated with the generation of tonal noise, ascribable to the perforated metal.

Further developments of the proposed methodology will evolve towards considering more complex geometries for the outer porous façade, where the tensorial formulation can be fully exploited to describe more complex interaction between the flow and the permeable elements. For example, when dealing with an expanded metal sheet, the CFD reduced order model must be able to describe the flow deviation that occurs and to do so the Darcy-Forchheimer model must rely on a full tensor, where 9 input parameters are to be identified.

**Author Contributions:** Methodology and conceptualization, G.P., O.B., P.S., L.R., A.Z.; software, L.R., G.P., O.B.; validation and visualization, G.P., O.B.; writing—original draft preparation, G.P.; writing—review and editing, P.S., A.Z.; supervision, P.S., A.Z. All authors have read and agreed to the published version of the manuscript.

**Funding:** This research received no external funding.



**Institutional Review Board Statement:** Not applicable.

**Informed Consent Statement:** Not applicable.

**Data Availability Statement:** Exclude this statement

**Conflicts of Interest:** The authors declare no conflict of interest.

### Abbreviations

The following abbreviations are used in this manuscript:

PDSF	Permeable Double Skin Façade
CFD	Computational Fluid Dynamics
WT	Wind Tunnel

### References

- Da Silva, F.M.; Gomes, M.G. Gap inner pressures in multi-storey double skin facades. *Energy Build.* **2008**, *40*, 1553–1559. [[CrossRef](#)]
- Gerhardt, H.; Kramer, C. Wind loads on wind-permeable building facades. *J. Wind Eng. Ind. Aerodyn.* **1983**, *11*, 1–20. [[CrossRef](#)]
- Kemper, F.; Feldmann, M. Wind load assumptions for permeable cladding elements considering the installation context. *J. Wind Eng. Ind. Aerodyn.* **2019**, *184*, 277–288. [[CrossRef](#)]
- Pomaranzi, G.; Daniotti, N.; Schito, P.; Rosa, L.; Zasso, A. Experimental assessment of the effects of a porous double skin façade system on cladding loads. *J. Wind Eng. Ind. Aerodyn.* **2020**, *196*, 104019. [[CrossRef](#)]
- Zasso, A.; Perotti, F.; Rosa, L.; Schito, P.; Pomaranzi, G.; Daniotti, N. Wind Pressure Distribution on a Porous Double Skin Façade System. In *Proceedings of the Italian Association for Wind Engineering, 2018—INVENTO Conference*; Springer: Cham, Switzerland, 2018; pp. 730–741.
- Lo, Y.L.; Wu, Y.T.; Fu, C.L.; Yu, Y.C. Wind load reduction effects on inner buildings by exterior porous façades. *Build. Environ.* **2020**, *183*, 107148. [[CrossRef](#)]
- Jones, N.L.; Goehring, A. Aeroacoustic facade noise: Predicting wind-induced noise from perforated facade panels. In *Proceedings of the 2018 Building Performance Analysis Conference and SimBuild Co-Organized by ASHRAE and IBPSA-USA, Chicago, IL, USA, 26–28 September 2018*; pp. 274–281.
- Feichtner, A.; Mackay, E.; Tabor, G.; Thies, P.R.; Johanning, L. Comparison of Macro-Scale Porosity Implementations for CFD Modelling of Wave Interaction with Thin Porous Structures. *J. Mar. Sci. Eng.* **2021**, *9*, 150. [[CrossRef](#)]
- Xu, M.; Patruno, L.; Lo, Y.L.; de Miranda, S. On the use of the pressure jump approach for the simulation of separated external flows around porous structures: A forward facing step. *J. Wind Eng. Ind. Aerodyn.* **2020**, *207*, 104377. [[CrossRef](#)]
- Arghode, V.K.; Joshi, Y. Modeling strategies for air flow through perforated tiles in a data center. *IEEE Trans. Compon. Packag. Manuf. Technol.* **2013**, *3*, 800–810. [[CrossRef](#)]
- Shen, X.; Wang, T.; Zhong, W. Numerical Simulation and Wake Modeling of Wind Turbine Rotor as AN Actuator Disk. *Int. J. Mod. Phys. Conf. Ser. World Sci.* **2012**, *19*, 320–330. [[CrossRef](#)]
- Feichtner, A.; Mackay, E.; Tabor, G.; Thies, P.R.; Johanning, L.; Ning, D. Using a porous-media approach for CFD modelling of wave interaction with thin perforated structures. *J. Ocean Eng. Mar. Energy* **2021**, *7*, 1–23. [[CrossRef](#)]
- Feichtner, A.; Mackay, E.; Tabor, G.; Thies, P.R.; Johanning, L. Modelling wave interaction with thin porous structures using OpenFOAM. In *Proceedings of the 13th European Wave and Tidal Energy Conference (EWTEC 2019), Napoli, Italy, 1–6 September 2019*.
- Feng, L. Tone-like signal in the wind-induced noise of perforated plates. *Acta Acust. United Acust.* **2012**, *98*, 188–194. [[CrossRef](#)]
- Richards, P.; Robinson, M. Wind loads on porous structures. *J. Wind Eng. Ind. Aerodyn.* **1999**, *83*, 455–465. [[CrossRef](#)]
- Chen, H.; Christensen, E.D. Investigations on the porous resistance coefficients for fishing net structures. *J. Fluids Struct.* **2016**, *65*, 76–107. [[CrossRef](#)]
- Zasso, A.; Schito, P.; Rocchi, D. Experimental and Numerical Study of the Pressure Distribution on Allow Rise Building (CC). In *Proceedings of the 5th European & African Conference on Wind Engineering, Florence, Italy, 19–23 July 2009*; pp. 1000–1004.
- Cook, N.; Mayne, J. A novel working approach to the assessment of wind loads for equivalent static design. *J. Wind Eng. Ind. Aerodyn.* **1979**, *4*, 149–164. [[CrossRef](#)]
- Lawson, T. The design of cladding. *Build. Environ.* **1976**, *11*, 37–38. [[CrossRef](#)]
- Holmes, J.D. Equivalent time averaging in wind engineering. *J. Wind Eng. Ind. Aerodyn.* **1997**, *72*, 411–419. [[CrossRef](#)]
- Newberry, C.W.; Eaton, K.J.; Mayne, J. *Wind Loading on Tall Buildings: Further Results from Royex House*; Building Research Establishment: Watford, UK, 1973.
- Peng, X.; Yang, L.; Gavanski, E.; Gurley, K.; Prevatt, D. A comparison of methods to estimate peak wind loads on buildings. *J. Wind Eng. Ind. Aerodyn.* **2014**, *126*, 11–23. [[CrossRef](#)]